

Synthesis, Crystal Structure, Spectroscopic, Magnetic, Theoretical, and Microbiological Studies of a Nickel(II) Complex of L-Tyrosine and Imidazole, $[\text{Ni}(\text{Im})_2(\text{L-tyr})_2] \cdot 4\text{H}_2\text{O}$

Agnieszka Wojciechowska,^{*,†} Marek Daszkiewicz,[‡] Zbigniew Staszak,[§] Agnieszka Trusz-Zdybek,^{||} Alina Bieńko,[⊥] and Andrzej Ozarowski^{||}

[†]Faculty of Chemistry, [§]Institute of Informatics, ^{||}Institute of Environment Protection Engineering, Wrocław University of Technology, Wybrzeże Wyspiańskiego 27, 50-370 Wrocław, Poland

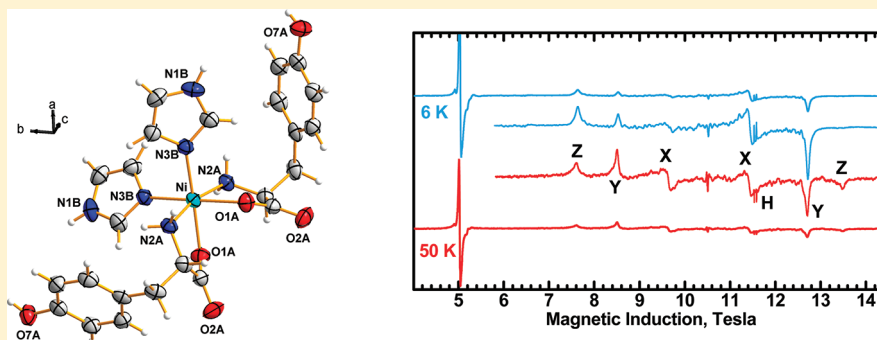
[‡]Institute of Low Temperature and Structure Research, Polish Academy of Sciences, Okólna 2, 50-422 Wrocław, Poland

[⊥]Faculty of Chemistry, University of Wrocław, 14 F. Joliot-Curie, 50-383 Wrocław, Poland

[§]National High Magnetic Field Laboratory, Florida State University, 1800 East Paul Dirac Drive, Tallahassee, Florida 32310, United States

Supporting Information

ABSTRACT:



The $[\text{Ni}(\text{Im})_2(\text{L-tyr})_2] \cdot 4\text{H}_2\text{O}$ (**1**) complex was obtained in crystalline form as a product of interaction of L-tyrosine sodium salt, imidazole, and NiSO_4 . The X-ray structure was determined, and the spectral (IR, FIR, NIR–vis–UV, HF EPR) and magnetic properties were studied. The Ni^{2+} ion is hexacoordinated by the N and O atoms from two L-tyrosine molecules and by two N atoms of imidazole, resulting in a slightly distorted octahedral $[\text{NiN}_2\text{N}_2'\text{O}_2]$ geometry with a tetragonality parameter $T = 0.995$. The bands observed in the electronic spectra were ascribed to the six spin-allowed electronic transitions ${}^3\text{B}_{1g} \rightarrow {}^3\text{E}_g$ and ${}^3\text{B}_{2g}, {}^3\text{B}_{1g} \rightarrow {}^3\text{A}_{2g}$ and ${}^3\text{E}_g$, and ${}^3\text{B}_{1g} \rightarrow {}^3\text{A}_{2g}$ and ${}^3\text{E}_g$. The spin Hamiltonian parameters g , D , and E , which were determined from high-field HF EPR spectra, excellently reproduced the magnetic properties of the complex. Calculation of the zero-field splitting in the $S = 1$ state of nickel(II) using DFT and UHF was attempted. The biological activity of the complexes has been tested for antifungal and antibacterial effects against *Aspergillus flavus*, *Fusarium solani*, *Penicillium verrucosum*, *Bacillus subtilis*, *Serratia marcescens*, *Pseudomonas fluorescens*, and *Escherichia coli*.

INTRODUCTION

In recent studies focused on the transition-metal complexes of L-tyrosine [L-tyr; 2-amino-3-(4-hydroxyphenyl)propanoic acid] and its isomers, structural, thermodynamic, spectral, and kinetic methods have been widely applied to characterize their physicochemical properties.^{1–7} In general, L-tyrosine and its derivatives bond to metal centers by the amino N atom, carboxylate O atoms, and phenolate O atom. The carboxylate groups can coordinate to a metal ion in a monodentate,⁵ chelate,⁶ or bridging fashion,⁷ depending on their physicochemical properties.^{1–7}

The first L-tyrosinatonicel(II) complex, $[\text{Ni}(\text{L-tyr})_2(\text{H}_2\text{O})_2] \cdot \text{CH}_3\text{OH}$, was investigated by Hamalainen and co-workers in

1977.¹ The Cambridge Structural Database (CSD)⁸ contains only three Ni^{2+} complexes with unsubstituted L-tyrosine^{1,9} and one with its derivative.¹⁰ In those monomeric compounds, L-tyrosine shows typical chelating coordination via the amino N atom and one of the carboxylate O atoms. The Ni^{2+} ions are hexacoordinated in three other complexes exhibiting the pseudooctahedral geometry,^{1,9} and only one Ni^{2+} ion complex with a L-tyrosine derivative has the square-planar geometry.¹⁰ Thermodynamic characterization of nickel(II) complex formation in aqueous–ethanolic solutions, recently reported by Molchanov

Received: July 12, 2011

Published: October 19, 2011

and Ledenkov,³ showed changes of $\log K$ upon solvation of the amino and carboxylate groups of the tyrosine anion. This suggests the chelating coordination of this acid to Ni^{2+} ion, while the phenolate O-atom coordination appears to be unlikely.

Metal complexes play an important role in regulating biological activities. Many coordination compounds present activity against tuberculosis, influenza, and rheumatism or are suggested as pesticides and fungicides. L-Tyrosine complexes of di- and trivalent metal ions (i.e., Zn^{2+} , Sn^{2+} , Hg^{2+} , Cd^{2+} , Cr^{3+} , Fe^{3+} , La^3 , Eu^{3+}) exhibit, aside from their interesting structural,^{7,dg} spectroscopic,^{7a} magnetic,⁷ and thermodynamic³ properties, curious antibacterial and antifungal activity.¹¹ This activity was one reason that these complexes have been used as components of ointments and disinfectants. However, we have found no literature reports on the crystal structure and spectroscopic characterization combined with the biological activity of nickel(II) complexes with L-tyrosine.

In this work, we present the full X-ray structure determination, spectroscopic far-IR (FIR), IR, near-IR (NIR)–vis–UV, and high-frequency electron paramagnetic resonance (HF EPR) studies, as well as magnetic characterization of a new hexacoordinated nickel(II) complex containing imidazole and L-tyrosine, $[\text{Ni}(\text{Im})_2(\text{L-tyr})_2] \cdot 4\text{H}_2\text{O}$ (**1**). The experimental EPR data were compared to the results of theoretical studies such as the density functional theory (DFT) calculation. Aside from the structural, spectroscopic, and magnetic properties, we present here a study of the antibacterial and antifungal properties of free L-tyrosine and imidazole, of the $[\text{Cu}(\text{L-tyr})_2]_n$ and $[\text{Ni}(\text{L-tyr})_2(\text{H}_2\text{O})_2] \cdot \text{H}_2\text{O}$ complexes as well as of the title complex **1**. We have reported earlier syntheses as well as the structural, spectroscopic, and magnetic properties of the $[\text{Cu}(\text{L-tyr})_2]_n$ complex,^{7a} whereas the crystal structure of $[\text{Ni}(\text{L-tyr})_2(\text{H}_2\text{O})_2] \cdot \text{H}_2\text{O}$ has been published by Hamalainen and co-workers.^{9a}

EXPERIMENTAL SECTION

Synthesis of Complex $[\text{Ni}(\text{Im})_2(\text{L-tyr})_2] \cdot 4\text{H}_2\text{O}$ (1**).** A total of 10 mL of a 0.01 M aqueous solution of NiCl_2 was slowly mixed with 20 mL of a 0.01 M aqueous solution of disodium L-tyrosinate. After 1 h, 20 mL of a 0.01 M aqueous solution of imidazole was added dropwise. The mixture was slowly evaporated at room temperature, and deep-blue crystals of complex **1** were obtained within 1 month. The crystals were filtered, washed with water, and dried in a desiccator over P_4O_{10} . Anal. Calcd for $\text{C}_{24}\text{H}_{36}\text{N}_6\text{O}_{10}\text{Ni}$ (MW 627.30): C, 45.95; H, 5.79; N, 13.40; O, 25.51; Ni, 9.36. Found: C, 45.0; H, 5.55; N, 13.15; O, 25.85; Ni, 9.45. All of the chemicals were of reagent grade and were used as received. L-Tyrosine disodium salt and imidazole were obtained from Sigma, and NiCl_2 was purchased from Merck.

Synthesis of Complex $[\text{Ni}(\text{L-tyr})_2(\text{H}_2\text{O})_2] \cdot \text{H}_2\text{O}$. A total of 10 mL of a 0.1 M aqueous solution of NiCl_2 was slowly added to 20 mL of a 0.1 M aqueous solution of disodium L-tyrosinate. Pearl-blue plates crystallized within 3 days. The product identity was confirmed by single-crystal X-ray determination of the unit cell parameters, which were in accordance with those reported by Hamalainen et al.^{9a}

Crystallography. The X-ray diffraction data were collected on a KUMA Diffraction KM-4 four-circle single-crystal diffractometer equipped with a CCD detector, using graphite-monochromated $\text{Mo K}\alpha$ radiation ($\lambda = 0.71073 \text{ \AA}$). The raw data were integrated with the CrysAlis Data Reduction Program (version 1.172.32.6) taking into account absorption correction.¹² Reflection intensities were corrected for the Lorentz and polarization effects. The crystal structure was solved by direct methods¹³ and refined by the full-matrix least-squares method using the SHELXL-97 program.¹⁴ Non-H atoms were

refined with anisotropic displacement parameters. H atoms were located from the difference Fourier maps and refined assuming a “ride-on” model.

Physicochemical and Spectroscopic Studies. Elemental analysis for nickel was performed by the inductively coupled plasma atomic emission spectrometry (ICP-AES) method and that for carbon, hydrogen, and nitrogen by the Kumpan method. IR spectra over the range $4000\text{--}50 \text{ cm}^{-1}$ were recorded in KBr pellets or Nujol mulls using the Perkin-Elmer FTIR-2000 and 1600 spectrophotometers. The NIR–vis–UV electronic spectra were obtained on a Cary 500 scan spectrophotometer over the range $5000\text{--}50\,000 \text{ cm}^{-1}$ with a resolution of 10 cm^{-1} . Solid-state reflectance spectra were measured for both L-tyrosine disodium salt (**L1**) and imidazole (**L2**). Reflectance and absorbance electronic spectra of **1** were obtained at 293 K for both single crystals and solutions in dimethyl sulfoxide (DMSO). The variable digital filter method with parameters step = 50, $\alpha = 200$, and $N = 20$ was applied in order to obtain the approximate band positions for spectral analysis.^{15a,b}

The variable digital filter method described by Bierman and Ziegler^{15c} was used for analytical purposes and later adopted for analysis of the electronic and vibrational spectra.^{15a,b} The filter acts as a single convolution of the spectral points measured at equal steps with a filter function $a(n)$:

$$T(k) = \sum_{n=-N}^N a(n) f(k-n)$$

where $a(n) = (2\alpha + 1)/(2N + 1) - 2\alpha|n|/N(N + 1)$, where N is the actual number of the sum component ($-N < n < N$), $T(k)$ is the filtered value in the k th measured point, f is the unfiltered spectrum, N is the filter width, and α is a real number determining the degree of the resolution enhancement. By varying α and N , one can achieve different degrees of noise reduction, an increase of height, and a decrease of the width of the component bands.

EPR and Magnetic Measurements. High-field HF EPR spectra at temperatures ranging from ca. 6 to 290 K were recorded on a home-built spectrometer at the EMR facility of the NRMFL.¹⁶ The instrument is a transmission-type device in which microwaves are propagated in cylindrical lightpipes. The microwaves were generated by a phase-locked Virginia Diodes source generating frequency of $13 \pm 1 \text{ GHz}$ and producing its harmonics of which the 2nd, 4th, 6th, 8th, 16th, 24th, and 32nd were available. A superconducting magnet (Oxford Instruments) capable of reaching a field of 17 T was employed. The sample (50 mg) was very carefully ground, yet effects of the microcrystals were still observed as false noise seen within the spectrum but not outside (Figures 5 and 6). The powder sample was not constrained and showed no magnetic torquing at high magnetic fields.

Magnetic susceptibility measurements over the temperature range 1.8–300 K were performed at a magnetic field of 0.5 T using a Quantum Design SQUID-based MPMSXL-5-type magnetometer, which was calibrated with a 99.9985% palladium rod sample (Materials Research Corp.). Correction for the sample holder, as well as the diamagnetic correction χ_D , which was estimated from the Pascal constants,¹⁷ was applied. A temperature-independent paramagnetism of $60 \times 10^{-6} \text{ cm}^3 \text{ mol}^{-1} \text{ K}$ for nickel(II) was used in the calculations. The magnetization measurements were conducted at 2 K, with the magnetic field varying from 0 to 5 T.

Microbiological Investigation. The filter paper disk method was employed for the *in vitro* study of antibacterial effects against *Bacillus subtilis*, *Serratia marcescens*, *Pseudomonas fluorescens*, and *Escherichia coli*. Additionally, the antifungal properties of our compounds were tested on *Aspergillus flavus*, *Fusarium solani*, and *Penicillium verrucosum*. This method is based on diffusion of a metal complex solution from a filter paper disk through the solidified culture media on a Petri dish

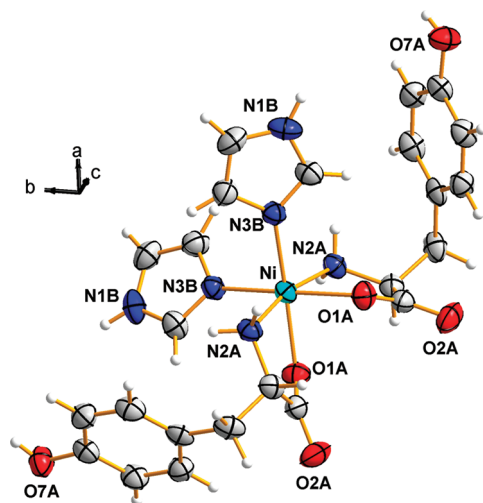


Figure 1. Coordination sphere of the Ni^{II} ion in 1.

and measurement of the zone around the filter paper in which the growth of microorganisms is inhibited entirely.

The strains of bacteria and fungi were stored on a nutrient agar medium and a Sabouraud agar medium with chloramphenicol, respectively, at 4 °C.

Before the tests, the isolates of bacteria and fungi were seeded in tubes with a nutrient broth and a liquid Sabouraud medium with chloramphenicol, respectively. The solutions were incubated in a thermostat at 25 °C for 24 h. The seeded inoculum of microorganisms (1 mL) was homogenized in the tubes with melted media (9 mL) at 45 °C. Subsequently, the homogeneous suspensions were poured into Petri dishes and cooled. The disks of filter paper (4 mm diameter) were placed on top of the solidified media and were saturated by solutions of each complex (20 μ L of 2×10^{-5} dm³). The disks containing only DMSO were used as controls. The plates were incubated at 25 °C for 24 h. The inhibitory activity was measured as the diameter (in millimeters) of the observed inhibition zones (see the Supporting Information). The tests were repeated to confirm the findings, and the average readings were taken. An inhibition zone diameter over 7 mm indicates that a tested compound is active against the bacteria and fungi under investigation. The concentration of each solution was 1.0×10^{-3} M, and commercially available DMSO was employed to dissolve the samples.¹¹ DMSO has been routinely used in bacterial and fungal tests of free L-tyrosine and imidazole, and their compounds have been reported previously as well as, for the complex $[\text{Ni}(\text{Im})_2(\text{L-tyr})_2] \cdot 4\text{H}_2\text{O}$ investigated here.

RESULTS AND DISCUSSION

Crystal Structure of $[\text{Ni}(\text{Im})_2(\text{L-tyr})_2] \cdot 4\text{H}_2\text{O}$ (1). The compound crystallizes in the noncentrosymmetric space group of tetragonal symmetry, $P4_12_12_1$. The Ni^{II} ion occupies a special position on the 2-fold axis, and therefore its $[\text{N}_2\text{N}_2'\text{O}_2]$ coordination sphere has C_2 point group symmetry (Figure 1).

The coordination sphere around the Ni²⁺ ion consists of the N and O atoms from two L-tyrosine anions, completed by the two N atoms of imidazole molecules, resulting in the $[\text{NiN}_2\text{N}_2'\text{O}_2]$ chromophore of octahedral geometry. The two O atoms coordinate in cis position, similar to the N atoms of imidazoles. However, the two N atoms of the pending amino groups of the L-tyrosine anions occupy the trans positions. This particular arrangement of the coordination sphere is required for C_2 point group symmetry. The Ni–O and Ni–N bond lengths are slightly different; however, they are comparable to other hexacoordinated

Table 1. Experimental Bond Lengths (Angstroms) and Bond Angles (Degrees) of Complex 1^a

Ni–N3B	2.0703(16)
Ni–O1A	2.0894(14)
Ni–N2A	2.0905(16)
C1A–O1A	1.269(2)
C1A–O2A	1.236(2)
N3B–Ni–N3B ⁽ⁱ⁾	91.09(9)
N3B–Ni–O1A	173.20(6)
N3B–Ni–O1A ⁽ⁱ⁾	91.21(6)
O1A–Ni–O1A ⁽ⁱ⁾	87.24(8)
N3B–Ni–N2A	94.22(6)
O1A–Ni–N2A	79.22(6)
O1A ⁽ⁱ⁾ –Ni–N2A	91.93(6)
N3B–Ni–N2A ⁽ⁱ⁾	94.28(6)
O1A–Ni–N2A ⁽ⁱ⁾	91.93(6)
O1A ⁽ⁱ⁾ –Ni–N2A ⁽ⁱ⁾	79.22(6)
N2A–Ni–N2A ⁽ⁱ⁾	167.85(10)

^a Symmetry transformations used to generate equivalent atoms: (i) $y, x, -z$.

Table 2. Intermolecular Hydrogen Bonds Observed in Complex 1 (Angstroms and Degrees)^a

D–H...A	$d(\text{D–H})$	$d(\text{H}\cdots\text{A})$	$d(\text{D}\cdots\text{A})$	$\angle\text{DHA}$
N1B–H1B...O1W	0.86	1.93	2.789(3)	177.5
O1W–H1W1...O2A ⁽ⁱⁱ⁾	0.91	1.76	2.653(2)	165.0
O7A–H7A...O2W ⁽ⁱⁱⁱ⁾	0.82	1.89	2.691(2)	167.1
O2W–H1W2...O1A ⁽ⁱⁱ⁾	0.83	1.91	2.748(2)	176.3
O1W–H2W1...O7A ⁽ⁱ⁾	0.89	2.43	2.999(3)	121.7
O2W–H2W2...O1W ^(v)	0.83	2.63	3.105(2)	118.1
N2A–H2A1...O7A ⁽ⁱⁱ⁾	0.90	2.37	3.223(2)	158.4
O2W–H2W2...O7A ^(vi)	0.83	2.63	3.235(2)	163.6

^a Symmetry transformations used to generate the equivalent atoms: (i) $y, x, -z$, (ii) $-y + 1/2, x + 1/2, z + 1/4$, (iii) $y - 1/2, -x + 3/2, z - 1/4$, (vi) $y, x + 1, -z$, and (v) $x + 3/2, y + 1/2, -z + 1/4$.

nickel(II) complexes with L-tyrosine (Table 1),^{1,10} whereas the Ni–N_{imidazole} distances are slightly shorter than those found in another nickel(II) complex with cis-coordinated imidazole, $[\text{Ni}(\text{HM})_2(\text{Im})_2]$, where HM is mandelic acid (an α -hydroxy-carboxylic acid).¹⁸

The axial octahedron sites are occupied by two amino N2A atoms, while the two imidazole N3B and two carboxylate O1A atoms form a basal plane. However, the O1A atoms lie slightly out of this plane, which is reflected in the O1A–Ni–N2A chelate angle of 79.22(6)°. Additionally, the nonlinearity of the N2A–Ni–N2A entity (167.85°) is worth mentioning. The average in-plane distances Ni–N3B and Ni–O1A [2.0703(16) and 2.0894(14) Å] as well as the corresponding average out-of-plane axial bond length Ni–N2A [2.0905(16) Å] result in a tetragonality parameter $T = 0.995$ (where $T = R_{\text{int}}/R_{\text{out}}$ ¹⁹). Slight elongation of the Ni²⁺ ion octahedral geometry is seen in the slightly shorter Ni–N_{imidazole} distances in comparison with other bond lengths.

The monodentately coordinated carboxylate group of L-tyrosine exhibits slightly shorter C–O distances compared to those found in the polymeric L-tyrosinato complex of Cu²⁺ reported previously (Table 1).^{7a}

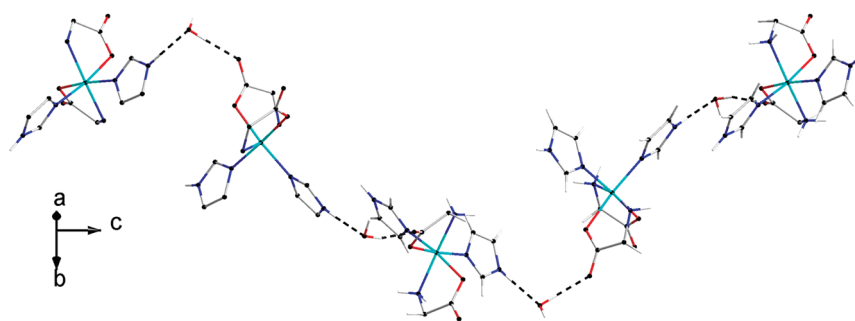


Figure 2. Helical hydrogen-bonding network around the 4_1 screw axis viewed down the $[210]$ axis. Some H atoms and residual groups of L-tyrosine were omitted for clarity.

The complex is monomeric, and the two shortest intermolecular distances between the nearest Ni^{2+} ions equal 9.380 and 9.862 Å. The next shortest distances are 11.133 and 13.280 Å. The water molecules are located between the layers, which are formed by the $[\text{Ni}(\text{Im})_2(\text{L-tyr})_2]$ units. The crystal packing of complex **1** is shown in the Supporting Information.

The atoms of $[\text{Ni}(\text{Im})_2(\text{tyr})_2]$ molecules are involved in a hydrogen-bonding network together with the H and O atoms of the water molecules. Table 2 presents the possible and intermolecular hydrogen-bond distances. It appears that the water molecules are very essential in creating the intermolecular interaction network because they participate in hydrogen bonds playing the role of both donors and acceptors. Acting as a donor, the O1W atom generates the hydrogen bonds O1W–H1W1 \cdots O2A⁽ⁱⁱ⁾ and O1W–H2W1 \cdots O7A⁽ⁱ⁾, with the latter being relatively weak. Those hydrogen bonds involve the uncoordinated O2A atom of the carboxylate group and the O7A atom of the hydroxyl group of the L-tyrosine residue. On the other hand, the O2W atom of the water molecule engages the coordinated O1A atom and forms the O2W–H1W2 \cdots O1A⁽ⁱⁱ⁾ hydrogen bond with a D \cdots A distance of 2.748(2) Å and a DHA angle of 176.3°. Both the coordinated and uncoordinated carboxylate O atoms of one L-tyrosine molecule act as acceptors in those hydrogen contacts. The O1W and O2W atoms of the water molecules are engaged as acceptors in the O7A–H7A \cdots O2W⁽ⁱⁱⁱ⁾ and N1B–H1B \cdots O1W hydrogen bonds to the O atom of the L-tyrosine ring hydroxyl group and the H atom on the imidazole N atom. The N1B–H1B \cdots O1W hydrogen bond is relatively weak as judged from the D \cdots A distance of 2.789(3) Å. In contrast to the N1B–H1B atoms of the imidazole, the N2A–H2A1 L-tyrosine amino group creates a very sensitive N2A–H2A1 \cdots O7A⁽ⁱⁱ⁾ contact with D \cdots A equal to 3.223(2) Å. We have found such a very weak hydrogen-bonding interaction of amino groups in our structure of $[\text{Cu}(\text{L-tyr})_2]_n$.^{7a}

However, in structure **1**, there are no hydrogen bonds designated by the unitary chain or unitary ring graph sets.²⁰ The shortest binary graph set $C_2^2(10)$ is formed by the imidazole N atom, the water molecule (O1W atom), and the carboxylate O atom. This contact arises from two hydrogen bonds, N1B–H1B \cdots O1W and O1W–H1W1 \cdots O2A⁽ⁱⁱ⁾. The hydrogen bonds exist along the 4_1 screw axis (Figure 2) in a sequence >a> b (see Table 2). This chain pattern, which is arranged around the screw axis, results in a right-handed turn helical structure. The other binary chain, $C_2^2(12)$, is created by the hydroxyl group, water molecules, and a carboxylate group in a sequence >d> e. However, the d and e hydrogen bonds are transformed only by a translation along the *a* axis, therefore resulting in a simple chain pattern.

The same descriptor, $C_2^2(12)$, designates the binary chain pattern of >b< *c* hydrogen bonds. This chain has a left-handed helical structure and propagates along the 2_1 screw axis, which is parallel to the *b* axis and is located at the position $1/4 + x, 1/8 + z$.

FIR, IR, and Raman Spectra. A very broad absorption in the frequency range 3100–3600 cm^{-1} corresponds to the $\nu(\text{O-H})$ vibration of the lattice (uncoordinated) water molecules, which are involved in a relatively weak (intermolecular) and a strong (intramolecular) hydrogen-bonding network in the crystals of **1**. Generally, in the range 2500–3500 cm^{-1} , the IR spectra of L-tyrosine salt and imidazole exhibit a large number of absorption bands, which correspond to the stretching NH and aromatic CH vibrations. The $\nu(\text{N-H})$ vibrations are distinctly observed in the IR spectrum of L-tyrosine as strong and sharp bands at 3585, 3559, 3362, and 3342 cm^{-1} . Those vibrations are correlated with the bands centered at 3125 and 3022 cm^{-1} in the imidazole spectrum. In the spectrum of complex **1**, a strong absorption correlated with the $\nu(\text{NH})$ vibration overlaps strongly with the weak bands assigned to the $\nu(\text{CH})$ vibration.

In the 1625–1550 cm^{-1} region, a very strong absorption with two maxima is observed in free L-tyrosine and in the title complex **1**. The maximum centered at 1600 cm^{-1} is assigned to the antisymmetric stretching vibration $\nu_{\text{as}}(\text{COO})$ of L-tyrosine. In the complex, this band is slightly shifted toward higher frequencies and appears at 1611 cm^{-1} . The spectral range 1400–1460 cm^{-1} is characteristic of the symmetric stretching vibration $\nu_{\text{sym}}(\text{COO})$. In this region in the L-tyrosine spectrum, we found only one band of medium intensity at 1425 cm^{-1} , with a slightly marked shoulder at ca. 1455 cm^{-1} , which is due to the symmetric carboxyl stretching mode $\nu_{\text{sym}}(\text{COO})$. Upon coordination of the carboxylate group to the Ni^{II} ion, this band splits into three bands of medium intensity located at 1454, 1434, and 1396 cm^{-1} . An analogous copper(II) complex of L-tyrosine exhibits these three components shifted toward higher energy.^{7a}

A reliable and useful spectroscopic criterion of the carboxylate coordination mode uses the energies of the antisymmetric and symmetric carboxyl stretching bands. The frequency difference $\Delta\nu(\text{COO}) = \nu_{\text{as}}(\text{COO}) - \nu_{\text{s}}(\text{COO})$ is a clue for recognition of the acetate bonding mode. The relations are $\Delta\nu_{\text{monodentate}}$ (much higher than 50 cm^{-1}) > $\Delta\nu_{\text{ionic}} \approx \Delta\nu_{\text{bridging}} > \Delta\nu_{\text{chelate}}$ (less than 50 cm^{-1}).^{21,22} In the studied complex, $\Delta\nu_{\text{ionic}}$ equals 175 cm^{-1} , whereas $\Delta\nu$ is 219 cm^{-1} . In a series of complexes with anions of α -hydroxycarboxylic acids like mandelate, benzylate, lactate, or glycolate, values of $\Delta\nu = \nu_{\text{as}}(\text{COO}) - \nu_{\text{sym}}(\text{COO})$ of ca. 200 cm^{-1} are typical for monodentate carboxylate groups.¹⁸ For the coordination mentioned above, the values of $\Delta\nu$ should be larger than $\Delta\nu_{\text{ionic}}$ by at least 50 cm^{-1} , but for **1**, the value of

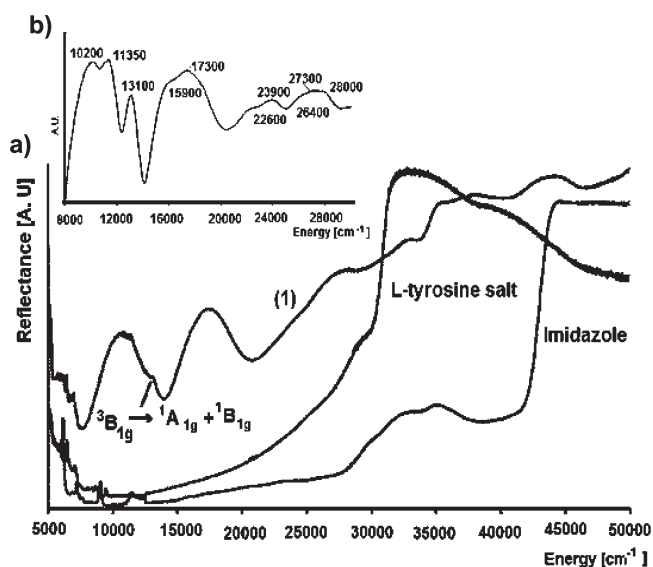


Figure 3. (a) NIR–vis–UV electronic diffuse-reflectance spectra of **1** and of the free ligands obtained at 298 K. (b) Filtered spectrum of complex **1** in the 8000–30 000 cm^{-1} spectral range.

$\Delta\nu$ is higher only by ca. 43 cm^{-1} than $\Delta\nu_{\text{ionic}}$. This suggests bridging coordination of the carboxylate group, while the crystal structure reveals a monodentate coordination. Such a small value of $\Delta\nu$ (43 cm^{-1}) is outside the monodentate coordination range and is probably caused by involvement of the coordinated and uncoordinated carboxylate O atoms in hydrogen bonds to the H atoms of the water molecules.

The $\delta(\text{NH}_2)$ vibration appears as an intense absorption at 1559 and 1592 cm^{-1} respectively in the IR spectra of L-tyrosine and the complex. We found this vibration as strong bands at 1581 and 1592 cm^{-1} in $[\text{Cu}(\text{tyr})_2]_n$.^{7a} The relatively strong double band with maxima centered at 1281 and 1267 cm^{-1} is assigned to the $\rho_r(\text{NH}_2)$ vibrations in L-tyrosine. The spectra of **1** and the pure amino acid show an intense band split into two components centered at 1256 and 1239 cm^{-1} . Additionally, in this energy region, a strong band originating from the imidazole ring-stretching modes is found at 1263 cm^{-1} in free imidazole.²³

In the FIR range, the imidazole molecule exhibits only three bands at 663, 623, and 144 cm^{-1} . The FIR spectrum of our complex **1** in the range 700–50 cm^{-1} is of poor quality, with unresolved bands. The L-tyrosine vibrations are prominent over most of the spectral range. Over the 700–600 cm^{-1} range, the acetate bending ν_9 and wagging ν_{14} appear in the FIR and Raman spectra of pure L-tyrosine salt as overlapped bands located at 645 and 624 cm^{-1} , respectively. However, detection of those weak-intensity bands in the spectrum of complex **1** is very difficult because of the presence of an imidazole vibration, which is found as a very strong band at 667 cm^{-1} , whereas this band was found at 663 cm^{-1} in the free imidazole spectrum. The very weak band at ca. 425 cm^{-1} could be assigned to the $\nu(\text{MN})$ vibration.

NIR–Vis–UV Electronic Spectroscopy

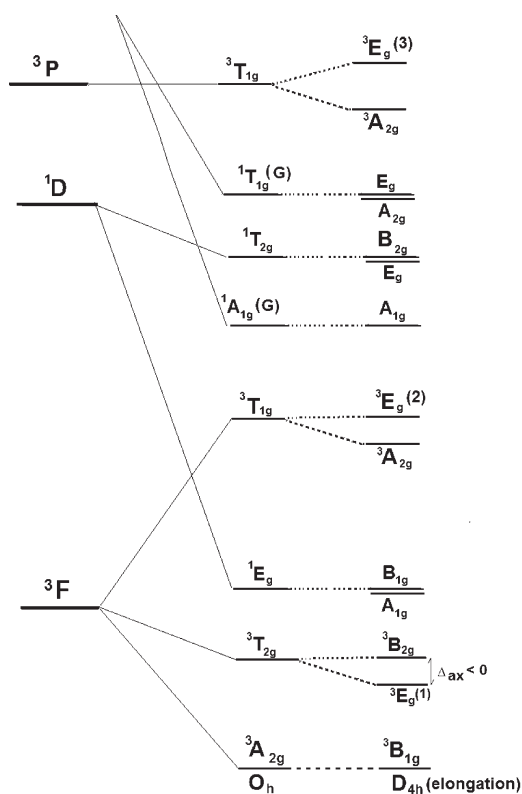
Solid-State Diffuse-Reflectance Spectra at 298 K. The solid-state diffuse-reflectance electronic spectra in the spectral range 5000–50 000 cm^{-1} of complex **1** and of each ligand are presented in Figure 3. In the region 7000–30 000 cm^{-1} , the spectrum of **1** exhibits low-intensity bands, which are attributed to the characteristic spin-allowed and spin-forbidden transitions of the Ni^{II} ion (d^8 configuration) in the pseudooctahedral crystal

Table 3. Values of the T Parameter for Octahedral L-Tyrosinatonicel(II) Complexes

complex	chromophore	T^a	ref
$[\text{Ni}(\text{Im})_2(\text{L-tyr})_2] \cdot 4\text{H}_2\text{O}$ (1)	$\text{NiN}_2\text{N}'_2\text{O}_2$	0.995	this work
$[\text{Ni}(\text{L-tyr})_2(\text{H}_2\text{O})_2] \cdot \text{H}_2\text{O}$	$\text{NiN}_2\text{O}_2\text{O}'_2$	0.985	9a
$[\text{Ni}(\text{L-tyr})(\text{C}_6\text{H}_{18}\text{N}_4)]\text{I} \cdot 2\text{H}_2\text{O}$	$\text{NiN}_2\text{N}'_2\text{O}_2$	0.973	9b
$[\text{Ni}(\text{L-tyr})(\text{H}_2\text{O})_2] \cdot \text{CH}_3\text{OH}$	$\text{NiN}_2\text{O}_2\text{O}'_2$	1	1

^a T is the tetragonality parameter where $T = R_{\text{int}}/R_{\text{out}}$ (R_{int} and R_{out} are the average in-plane and out-of-plane distances, respectively).

Scheme 1. Energy Levels of a Tetragonally Elongated Octahedral d^8 System (Energy Range 5000–30 000 cm^{-1})^{24,25}



field. The reflectance spectrum is very similar to the spectra of other pseudooctahedral $[\text{NiN}_2\text{N}'_2\text{O}_2]$ chromophores with trans-coordinated amino groups.²³ The first d–d transition is well seen as an asymmetric band at ca. 10 700 cm^{-1} . The maximum of the broad and asymmetric second d–d band is located at ca. 17 400 cm^{-1} . We could not clearly observe the third d–d band, whose maximum is estimated at ca. 27 900 cm^{-1} . The high-energy branch of this band is obscured by intense bands assigned to the intraligand and charge-transfer (CT) transitions. In the high-energy region 30 000–50 000 cm^{-1} , the spectrum shows unresolved absorptions with no clearly marked maxima.

The T parameter values for all hexacoordinated nickel(II) complexes of L-tyrosine that have been previously described are collected in Table 3. According to the crystal structure of **1**, two N atoms of imidazole as well as two N and two O atoms of L-tyrosine create a distorted *cis*- $\text{NiN}_2\text{N}'_2\text{O}_2$ octahedral chromophore around the Ni^{2+} ion with $T = 0.995$. Among the compounds collected in Table 3, the title complex **1** has the highest T , which implies only a slight deformation of the octahedral

Table 4. Splitting of the Terms of the d^8 Electronic Configuration Caused by the Symmetry Lowering from O_h (Ground State $^3A_{2g}$) to D_{4h} (Ground State $^3B_{1g}$) and the d–d Band Assignment for **1 in a Tetragonal Crystal Field^c**

O_h	$^3T_{2g}(^3F)$ (I d-d)	$^1E_g(^1D)$	$^3T_{1g}(^3F)$ (II d-d)	$^1T_{2g}(^1D)$	$^1A_{1g}(^1G), ^1T_{2g}(^1D)$	$^1T_{1g}(^1G)$	$^3T_{1g}(^3P)$ (III d-d)	Dq	Ds	Dt	B
D_{4h}	3E_g $^3B_{2g}$	$^1A_{1g}+^1B_{1g}$	$^3A_{2g}$ 3E_g	1E_g	$^1A_{1g}, ^1B_{2g}$	$^1A_{2g}$	$^3A_{2g}$ 3E_g				
Refl. ^a	10700	13100	17400	-	24000	-	27900				
^b	10200 11350	13100	15900 17300	22600	23900	26400	27300 28000	1130	434	132	865
Single Cryst. ^a	11500	12950	17200	-	-	-	-				
^b	10400 11800	13100*	16500 18100	22400	24000	26000	-	1180	472	145	886
Sol. ^{a,**}	9950 (29)	12950 (9)	16200 (27)	-	24950	-	28300				
^b	10050	13200	16500	20800	24550	-	28000				

^a Position taken from the spectrum. ^b Position taken from filtration (filter parameters: step = 50, α = 200, and N = 20). ^{*} Parameters: step = 50, α = 200, and N = 15. ^{**} Molar absorption coefficients ϵ ($\text{dm}^3 \text{mol}^{-1} \text{cm}^{-1}$) in parentheses. ^c The transition energies are given in cm^{-1} . Refl. = diffuse-reflectance spectrum; Single Cryst. = absorbance single-crystal spectrum at 295 K; Sol. = absorbance spectra in a DMSO solution.

geometry around the Ni^{II} ion. This slight deformation is clearly reflected in the asymmetric d–d bands. Unfortunately, no data concerning the d–d band energies or splitting for the remaining complexes collected in this table are available. The slight deformation of the octahedron in **1** implies a splitting of each d–d band into two components. The $^3A_{2g}$ term is the ground state for the d^8 configuration in octahedral crystal fields, and this becomes $^3B_{1g}$ in the D_{4h} symmetry. According to the energy level diagram (Scheme 1), in the D_{4h} symmetry, the $^3T_{2g}(^3F, O_h)$ state splits into 3E_g and $^3B_{2g}$, while $^3T_{1g}(^3F, O_h)$ splits into $^3A_{2g}$ and 3E_g . The third state, $^3T_{1g}(^3P, O_h)$ consists of $^3A_{2g}$ and 3E_g levels.²⁴ Those states are correlated with six spin-allowed transitions. Additional spin and symmetry-forbidden transitions become possible by splitting of the $^1E_g(^1D \text{ term}, O_h)$, $^1T_{2g}(^1D \text{ term}, O_h)$, and $^1T_{1g}(^1G \text{ term}, O_h)$ into $^1A_{1g} + ^1B_{1g}$, $^1E_g + ^1B_{2g}$, and $^1A_{2g} + ^1E_g$, respectively. The $^1A_{1g}(^1G \text{ term}, O_h)$ state is nondegenerate and keeps its symbol in D_{4h} .^{24,25} Finally, the $^1A_{1g}$ and $^1B_{1g}$ levels come from $^1E_g(^1G \text{ term}, O_h)$, whereas the 1E_g and $^1B_{2g}$ states arise from $^1T_{2g}(^1G \text{ term}, O_h)$.^{24,25}

Therefore, assuming a slightly elongated D_{4h} symmetry, the six observed components have been ascribed to the six spin-allowed electronic transitions $^3B_{1g} \rightarrow ^3E_g$ and $^3B_{1g} \rightarrow ^3B_{2g}$ (I d–d), $^3B_{1g} \rightarrow ^3A_{2g}$ and $^3B_{1g} \rightarrow ^3E_g$ (II d–d), and $^3B_{1g} \rightarrow ^3A_{2g}$ and $^3B_{1g} \rightarrow ^3E_g$ (III d–d) with energies of ca. 10 200, 11 350, 15 900, 17 300, 27 300, and 28 000 cm^{-1} , respectively. Additionally, a weak sharp peak at 13 100 cm^{-1} on the Ist d–d band arises from the symmetry and spin-forbidden $^3B_{1g} \rightarrow ^1A_{1g} + ^1B_{1g}$ transition (Scheme 1 and Figure 3). The successive spin-forbidden $^3B_{1g} \rightarrow ^1E_g + ^1B_{2g}$, $^3B_{1g} \rightarrow ^1A_{1g}$, and $^3B_{1g} \rightarrow ^1A_{2g} + ^1E_g$ transitions are correlated with the bands that appeared under the filtration process and are situated between the II and III d–d bands (Figure 3b and Table 4).

The high-energy branch of the III d–d band as well as the bands assigned to the spin and symmetry-forbidden $^3B_{1g} \rightarrow ^1A_{1g} + ^1B_{1g}$ and $^3B_{1g} \rightarrow ^1E_g + ^1B_{2g}$ transitions are obscured by CT transitions originating from imidazole ring orbitals $\pi_{1,2} \rightarrow \sigma^* \text{-Ni}^{26}$ and ligand-to-ligand CT $\pi-\pi^*$ and $n-\pi^*$ transitions in the L-tyrosine molecule.^{7a,11}

The energies of the six d-d transitions allowed compute the characteristic crystal-field parameters Dq, Ds, Dt, and Racah B. They are 1130, 434, 132, and 865 cm^{-1} , respectively (Table 4)

and stand in good agreement with the magnitudes observed for almost all nickel(II) complexes.^{24,26–28} For complex **1**, the value of 10Dq is directly correlated with the $^3B_{1g} \rightarrow ^3B_{2g}$ transition energy. This transition has higher energy than $^3B_{1g} \rightarrow ^3E_g$ because of the fact that the sign of the Dt parameter is positive and the axial ligand field should be weaker than the equatorial ligand field.

Absorbance Spectra (Single-Crystal and Solution Spectra at 293 K). In the single-crystal absorbance spectrum, the well-resolved asymmetric I and II d–d bands are centered at ca. 11 500 and 17 200 cm^{-1} (Figure 4 and Table 4). The expected III d–d band is obscured by the measurement noise. The filtration process revealed a splitting of each band into two components, as expected for the D_{4h} symmetry. The $^3B_{1g} \rightarrow ^3E_g$ and $^3B_{1g} \rightarrow ^3B_{2g}$ transitions are assigned as components of the I d–d band at 10 400 and 11 800 cm^{-1} , respectively. The splitting between the second d–d band components equals 1600 cm^{-1} , and the $^3B_{1g} \rightarrow ^3A_{2g}$ and $^3B_{1g} \rightarrow ^3E_g$ transitions correspond to the absorptions with maxima at 16 500 and 18 100 cm^{-1} , respectively. The crystal spectrum nicely exhibits a peak due to the first spin-forbidden $^3B_{1g} \rightarrow ^1A_{1g} + ^1B_{1g}$ transition (Scheme 1). This sharp peak is observed at 12 950 cm^{-1} , despite its small intensity, and it is red-shifted by 150 cm^{-1} compared to the reflectance spectra (Figure 4 and Table 4). This forbidden transition involves the $^1A_{1g}$ and $^1B_{1g}$ states. Unfortunately, even with the high sensitivity of the single-crystal measurement, no evidence of splitting of the $^1A_{1g}$ and $^1B_{1g}$ states could be found. The energy of the first component of the second forbidden transition ($^1T_{2g}$ in O_h) $^3B_{1g} \rightarrow ^1E_g$ equals 22 400 cm^{-1} (Figure 4 and Table 4). The positions of the succeeding spin-forbidden transitions $^3B_{1g} \rightarrow ^1A_{1g} + ^1B_{2g}$ and $^3B_{1g} \rightarrow ^1A_{2g}$ were found under the filtration process, giving the energies 24 000 and 26 000 cm^{-1} , respectively. A band associated with the $^3B_{1g} \rightarrow ^1E_g$ spin-forbidden transition ($^1T_{1g}$ in O_h) should be observed at ca. 30 000 cm^{-1} but is obscured by the III d–d band.²⁵

Calculations using the energies of the first four spin-allowed 3E_g , $^3B_{2g}$, $^3A_{2g}$, and 3E_g states obtained from the filtration process give the crystal-field parameters Dq = 1180 cm^{-1} , Ds = 472 cm^{-1} , Dt = 145 cm^{-1} , and B = 886 cm^{-1} (Table 4).^{25–27} These results seem to be reasonable and acceptable. Especially, the Dq value (1180 cm^{-1}) is very close to the 1186 cm^{-1} value characteristic

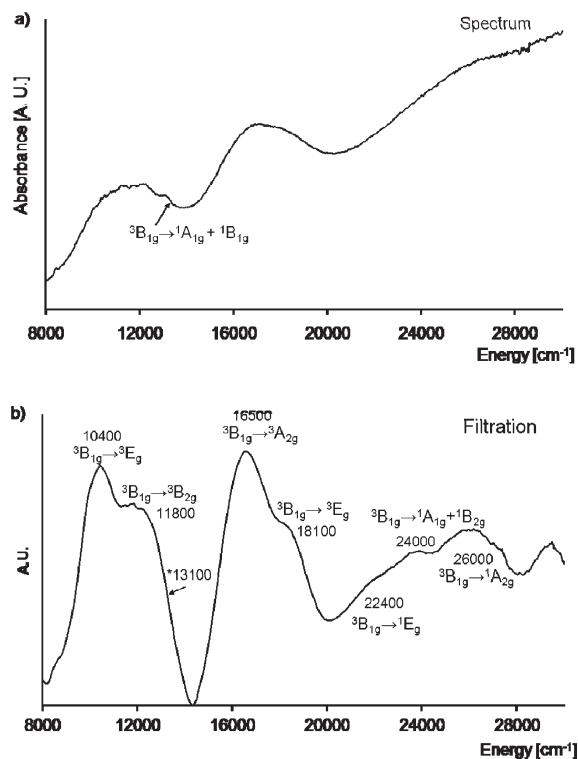


Figure 4. (a) Single-crystal absorbance spectrum of **1** obtained at 298 K. (b) Filtered spectrum and band assignment (* band that appears under the filter with step = 50, $\alpha = 200$, and $N = 15$).

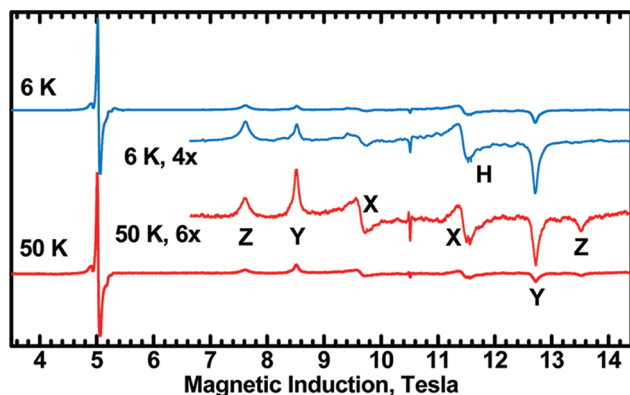


Figure 5. 324 GHz EPR spectra of **1** at the temperatures indicated. The molecular orientations for the respective transitions are marked with X, Y, and Z. Two sharp lines coming from a standard (H atoms trapped in an octaisobutylsilsesquioxane nanocage³¹) are marked with H. The strong line at 5.1 T is the so-called “half-field” forbidden transition $\Delta M_S = 2$ in the triplet ($S = 1$) spin state.

of the $[\text{N}_4\text{O}_2]$ chromophore and is higher, as expected, in comparison to 1077 cm^{-1} found for the $[\text{N}_2\text{O}_4]$ chromophore in our earlier studies.^{28,29}

In the solution spectrum, the maxima of the broad and almost symmetric d–d bands are centered at 9550 , 16200 , and 28300 cm^{-1} with ϵ over the range $30\text{--}180\text{ dm}^3\text{ mol}^{-1}\text{ cm}^{-1}$ (Table 4). The shoulders on the first and second d–d bands, which are well seen in reflectance and crystal spectra, are poorly resolved in this spectrum. Even the filtration process has not

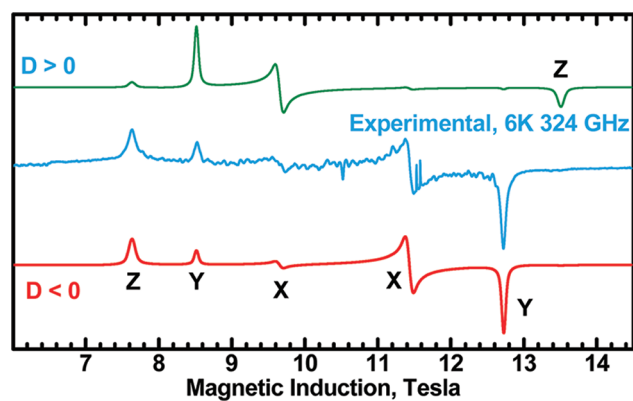


Figure 6. “Allowed” $\Delta M_S = 1$ part of the 324 GHz, 6 K EPR spectrum of **1**. Center: experimental. Top: simulated for $S = 1$ with $g_x = 2.168$, $g_y = 2.163$, $g_z = 2.188$, $D = +2.997\text{ cm}^{-1}$, and $E = +0.4066\text{ cm}^{-1}$. Bottom: simulated with the same g values and $D = -2.997\text{ cm}^{-1}$ and $E = -0.4066\text{ cm}^{-1}$.

given unequivocal evidence of d–d band splitting. This is in agreement with the T value of 0.995 reflecting a very small distortion from O_h symmetry and may suggest almost octahedral symmetry of the $[\text{Ni}(\text{Im})_2(\text{L-tyr})]^{2+}$ cation in solution, although the ϵ values appear to be too high for the O_h geometry.

High-Field HF EPR. Well-resolved high-field EPR spectra of a triplet state ($S = 1$) were observed over the microwave frequency range $100\text{--}416\text{ GHz}$ (Figures 5 and 6). They were interpreted in terms of the spin Hamiltonian

$$\hat{H} = \mu_B B \cdot g \cdot \hat{S} + D\{\hat{S}_z^2 - (1/3)S(S+1)\} + E(\hat{S}_x^2 - \hat{S}_y^2) \quad (1)$$

Simulations of the powder patterns, which used full diagonalization of the spin-Hamiltonian matrix, allowed one to determine the parameters $g_x = 2.170$, $g_y = 2.166$, $g_z = 2.193$, $D = -3.010\text{ cm}^{-1}$, and $E = -0.4066\text{ cm}^{-1}$ at 50 K. The parameters were slightly temperature-dependent, changing at 5 K to $g_x = 2.168$, $g_y = 2.163$, $g_z = 2.188$, $D = -2.997\text{ cm}^{-1}$, and $E = -0.4066\text{ cm}^{-1}$. The sign of the zero-field-splitting (zfs) parameter D can be unambiguously determined from high-field EPR spectra thanks to the Zeeman splitting being comparable to or larger than kT .³⁰ With D negative, as in the present case, the high-field “parallel” and the low-field “perpendicular” transitions of a triplet spectrum (marked with Z and X, Y, respectively, in Figures 5 and 6) are “frozen out” at low temperatures, while the opposite would occur for a positive D (Figure 6). Knowledge of the zfs parameters and their signs is useful in interpreting the magnetic susceptibility data. The D magnitude is moderate for Ni^{2+} because it may vary between $+3$ ³³ and -10 cm^{-1} ³⁴ for Ni^{2+} in $[\text{N}_4\text{O}_2]$ coordination.

Magnetic Properties. The magnetic susceptibility measurements were performed over the temperature range $1.80\text{--}300\text{ K}$. The experimental data, plotted as thermal variations of the effective magnetic moment, are shown in Figure 7. The magnetic susceptibility increases with decreasing temperature, exhibiting at not too low temperatures the Curie–Weiss behavior with a Curie constant C of $1.19\text{ cm}^3\text{ mol}^{-1}$ and a Weiss constant $\Theta = -0.17\text{ K}$. At room temperature, $\chi_M T$ equals $1.19\text{ cm}^3\text{ K mol}^{-1}$, corresponding to the magnetic moment of $3.08\mu_B$, as expected for an uncoupled Ni^{II} ion. The magnetic moments, as well as the

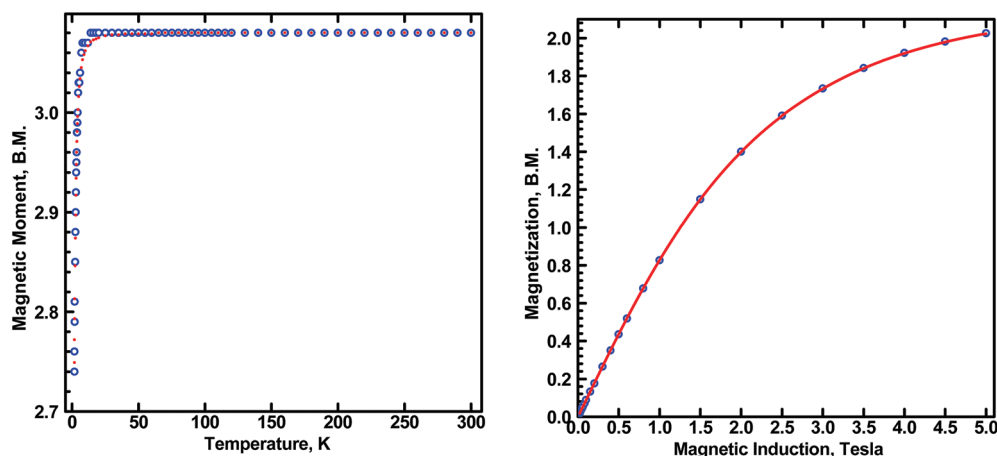


Figure 7. (a) Temperature dependence of the effective magnetic moment of complex 1. Open circles: experimental. Dots: calculated with $g_x = 2.168$, $g_y = 2.163$, $g_z = 2.188$, $D = -2.997 \text{ cm}^{-1}$, and $E = -0.4066 \text{ cm}^{-1}$. (b) Field dependence of magnetization for complex 1 at 2 K. Circles: experimental. Solid line: calculated with the same parameters as above.

product $\chi_M T$ decrease smoothly over a wide temperature range and subsequently decrease rapidly at the lowest temperatures to $0.94 \text{ cm}^3 \text{ mol}^{-1} \text{ K}$ ($2.74 \mu_B$) at 1.8 K. This decrease of $\chi_M T$ can be due to the zfs effect on Ni^{II} ions and/or to the intermolecular exchange interactions between the nearest-neighboring Ni^{II} ions in the crystal lattice. Because large zfs parameters $D = -2.997 \text{ cm}^{-1}$ and $E = -0.4066 \text{ cm}^{-1}$ were found from EPR at 5 K, their effect must be considered first. It is clear that the Curie–Weiss law, which requires kT be much larger than the zfs and Zeeman splitting, cannot be applied at the lowest temperatures: the thermal energy kT at 2 K (1.39 cm^{-1}) is smaller than the zfs, and the Zeeman energy of $\pm 0.5 \text{ cm}^{-1}$ at 5000 G for the $M_S = \pm 1$ levels is comparable to kT . Also, with large zfs, the energies of the $S = 1$ substates are nonlinear functions of the magnetic field (Figure S2 in the Supporting Information).

The magnetic susceptibility χ and magnetization M must therefore be calculated from the basic principles:

$$M = -N \frac{\sum_{i=1}^3 \frac{\partial E_i}{\partial B} \exp(-E_i/kT)}{\sum_{i=1}^3 \exp(-E_i/kT)} \quad (2)$$

and

$$\chi = M/B \quad (3)$$

No adjustable parameters were used in the analysis of both the temperature dependence of the magnetic susceptibility and magnetization at 1.8 K. The energies E_i of the three substates were found by diagonalizing the spin-Hamiltonian matrix with all g_x , g_y , g_z , D , and E parameters fixed as found from the EPR. The derivatives $\partial E_i/\partial B$ were calculated numerically by evaluating each E_i at two magnetic fields, 1 G above and 1 G below the working field ($B = 5000 \text{ G}$) of the SQUID magnetometer. The magnetizations or susceptibilities evaluated at the orientations X, Y, and Z were averaged. The effective magnetic moments, obtained from magnetic susceptibility, which was calculated on the basis of eqs 2 and 3 by using $\mu_{\text{eff}} = 2.83(\chi T)^{1/2}$, are compared to the experimental data in Figure 7a. The agreement is very good, with a factor $R = \sum(\mu_i^{\text{exp}} - \mu_i^{\text{calc}})^2 / \sum(\mu_i^{\text{exp}})^2$ equal to 3.2×10^{-6} .

For example, at 1.8 K, the experimental and calculated moments are 2.740 and 2.749, respectively. Thus, in our case the zfs and Zeeman splitting account for all of the variation of the magnetic moment or susceptibility, and there is no need for inclusion of any intermolecular exchange interactions into the data analysis.

The magnetization at 2 K as a function of the magnetic field between 0 and 5 T (Figure 7b) was also calculated from eq 2, showing very good agreement with the experimental data and thus confirming the zfs as the main factor determining the magnetic properties of our complex. The system under investigation can be viewed as a pseudochain, which is created by the hydrogen-bonding network formed by the imidazole N atom, the O1W atom of the water molecule, and the O atom of the carboxylate group. These contacts are accomplished by two $\text{N1B-H1B} \cdots \text{O1W}$ and $\text{O1W-H1W1} \cdots \text{O2A}^{(\text{ii})}$ hydrogen bonds. However, these bonds are apparently unable to provide a magnetic exchange pathway, possibly because of the rather long intermolecular Ni–Ni separations (9.380 and 9.862 Å).

An attempt was undertaken to evaluate the D parameter by the DFT method. The X-ray structure was used in calculations, and the free ORCA software was employed.³⁵ Calculations used the functional BP86 and the Ahlrichs-TZV function base.³⁵ Both the dipolar (spin–spin coupling) and spin–orbit coupling (SOC) contributions to zfs were taken into account, and the coupled-perturbed method was used for the latter. Contrary to the previous positive experience by some of us,^{36,37} this calculation brought very poor results. The estimated D value was 1 order of magnitude smaller than the experimental value. Also, the calculation underestimated the g -component deviations from the free-electron value. Both effects are symptoms of an underestimation of the SOC contribution. The zfs parameters are quantities that are very sensitive to the structure and approximations used and are difficult to model. Usage of the B3LYP functional offered no improvement. The failure of DFT to predict zfs in transition-metal complexes and a better behavior of the ab initio calculations was noticed previously.³⁸ Unrestricted Hartree–Fock calculations were therefore performed, again with ORCA, followed by calculation of the zfs by using the “coupled-perturbed” treatment of the SOC contribution. That proved to be incomparably more successful than DFT, resulting in $D = -2.5 \text{ cm}^{-1}$ and also giving better, although overestimated, g values. A comparison of the

Table 5. Comparison of the Experimental Spin-Hamiltonian Parameters to the Results of DFT and UHF Calculations

complex		exp.	DFT	UHF
[Ni(Im) ₂ (L-tyr) ₂]·4H ₂ O (1)	g_x, g_y, g_z	2.168, 2.163, 2.188	2.07, 2.07, 2.08	2.25, 2.26, 2.26
	D, E^a	−2.997, −0.407	−0.22, −0.042	−2.525, −0.194
[Ni(CMA) ₂ (Im) ₂ (MeOH) ₂] ²⁹	g_x, g_y, g_z	2.29, 2.18, 2.13	2.08, 2.09, 2.10	2.27, 2.31, 2.33
	D, E^a	5.77, 1.64	1.58, 0.18	5.43, 1.68
Fe(bt) ₂ (NCS) ₂ ³⁹	g_x, g_y, g_z	2.147, 2.166, 2.01	2.01, 2.03, 2.03	2.01, 2.15, 2.19
	D, E^a	12.43, 0.24	2.55, 0.26	9.91, 0.75
Co(PPh ₃) ₂ Cl ₂ ⁴⁰	g_x, g_y, g_z	2.166, 2.170, 2.240	2.07, 2.07, 2.08	2.27, 2.29, 2.52
	D, E^a	−14.66, 1.141	+2.78, +0.67	−22.68 ^b , 3.15

^a D and E are given in cm^{-1} . The sign of E is in accordance with the labeling of g_x and g_y , and would have to be reversed if g_x and g_y were swapped. ^b A better D value of -17.6 cm^{-1} was obtained from a multireference ab initio calculation.^{40b}

Table 6. Antifungal and Antibacterial Activity Data for L-Tyrosine Sodium Salt, Imidazole, and Their Metal Ion Complexes

	test fungus			test bacteria			
	<i>F. solani</i>	<i>A. flavus</i>	<i>P. verrucosum</i>	<i>E. coli</i>	<i>P. fluorescens</i>	<i>B. subtilis</i>	<i>S. marcescens</i>
	Mean Diameter of Inhibition (mm)						
DMSO	0	0	0	2 ^a	2 ^a	0	0
L-tyrosine sodium salt	4	10	8	6	2	1	2
imidazole	8	3	5	5	8	7	6
[Cu(L-tyr) ₂] _n ^{7a}	15 ^a	0	12 ^a	0	4 ^a	4 ^a	2 ^a
[Ni(L-tyr) ₂ (H ₂ O) ₂]·H ₂ O ^{9a}	9	4	15	2	3	3	2
[Ni(Im) ₂ (L-tyr) ₂]·4H ₂ O (1)	15 ^a	7 ^a	9	8	9	8	7

^a Growth of microorganisms in the inhibition zone.

DFT and UHF results for **1**, a related nickel(II)²⁹ as well as an iron(II)³⁹ and a high-spin cobalt(II)⁴⁰ complex with very large D is given in Table 5. A more traditional alternative method relates the components of the g and zfs tensors to the ligand-field energies that may be found from the electronic spectra.^{41,42} When working under a simplifying assumption of the D_{4h} symmetry, one gets⁴²

$$g_z = g_e - 2\lambda[4\kappa_z^2/\Delta_z(^3B_{1g} \rightarrow ^3B_{2g})]$$

$$g_{x,y} = g_e - 2\lambda[4\kappa_{x,y}^2/\Delta_{x,y}(^3B_{1g} \rightarrow ^3E_g)]$$

$$D = \lambda^2[4\kappa_{x,y}^2/\Delta_{x,y}(^3B_{1g} \rightarrow ^3E_g) - 4\kappa_z^2/\Delta_z(^3B_{1g} \rightarrow ^3B_{2g})]$$

where $\lambda = -315 \text{ cm}^{-1}$ is the SOC constant for Ni²⁺ and $\kappa_{x,y}$ and κ_z are the equatorial and axial orbital reduction factors whose deviation from 1 reflects the covalency.

To reconcile the g values with the electronic spectra, one has to assume $\kappa_{x,y}^2 = 0.66$ and $\kappa_z^2 = 0.84$. Then, $D = -3.69 \text{ cm}^{-1}$ is obtained from the formula above, in a reasonable agreement with the experiment. The g and D values are also correctly correlated by^{41,42} $D = (\lambda/2)(g_z - g_{x,y}) = -3.6 \text{ cm}^{-1}$ (vs experimental -3 cm^{-1}).

Microbiological Investigation. The antibacterial and antifungal properties of L-tyrosinato metal ion complexes have been reported earlier.^{11,43,44} A thorium(IV) complex containing L-tyrosine as a secondary ligand besides 8-hydroxyquinoline shows weak activity against strains of *Staphylococcus aureus* and *E. coli* compared to the antibacterial standard, tetracycline.⁴³ A L-tyrosinatonicel(II) complex exhibits moderate activity against the *B. subtilis*, *Streptococcus β-hemolytica*, *E. coli*, and *Shigella dysenteriae* in comparison to known antibacterial drugs like kanamycin. On the other hand, that complex presents very good

results of antifungal test when using *Aspergillus fumigates* and *Candida albicans*. The diameters of the inhibition zone equal 21 and 28 mm, respectively, while the inhibition zone of 0 mm diameter was found for a known antifungal drug, fluconazole.⁴⁴

In our investigation, the activity of L-tyrosine is highest against fungi as *A. flavus*. It affects to a lesser degree *P. verrucosum*. The [Ni(L-tyr)₂(H₂O)₂]·H₂O complex, as well as the free L-tyrosine, inhibit the growth of *P. verrucosum*. Additionally, this complex restrained the growth of *F. solani* to about 9 mm. However, both complexes [Cu(L-tyr)₂]_n and [Ni(L-tyr)₂(H₂O)₂]·H₂O are quite inactive against *A. flavus*. Besides that, the copper(II) compound is inactive against each of the three fungi. Pure imidazole is most active against *F. solani*, while it does not affect *A. flavus*. The title complex **1** is noticeably inactive against both fungi *F. solani* and *A. flavus*, but it increased markedly the inhibition zone of *P. verrucosum*.

The antibacterial tests using L-tyrosine, [Cu(L-tyr)₂]_n and [Ni(L-tyr)₂(H₂O)₂]·H₂O complexes against the bacterial strains of *B. subtilis*, *S. marcescens*, *P. fluorescens*, and *E. coli* gave rather poor results, with the inhibition zone diameter equal to or less than 7 mm (Table 6). L-Tyrosine is slightly active against *E. coli*, while the activity of pure imidazole extends over all four bacteria strains. **1** and the free imidazole are inhibitory factors for all four bacterial strains. Also, the antibacterial activity of **1** is definitely higher compared to that of [Ni(L-tyr)₂(H₂O)₂]·H₂O. Thus, the presence of imidazole molecules in complex **1** appears to enhance the antibacterial activity.

CONCLUSIONS

In summary, we synthesized and characterized structurally, spectroscopically, and magnetically a new octahedral Ni²⁺ ion

complex containing two biologically important ligands. In our complex, we found the smallest distortion of octahedral Ni^{2+} geometry among all nickel(II) complexes containing L-tyrosine. On the other hand, this small distortion is sufficient to affect the electronic d–d bands. The crystal-field parameters Dq , Ds , Dt , and B (1180, 472, 145, and 886 cm^{-1}) calculated from the energies of the first four spin-allowed 3E_g , ${}^3B_{2g}$, ${}^3A_{2g}$, and 3E_g states that were obtained from a single-crystal absorbance spectrum at 293 K are in accordance with those found for other $[\text{NiN}_4\text{O}_2]$ chromophores.

The spin-Hamiltonian parameters g_x , g_y , g_z , D , and E obtained from the high-field EPR could be reproduced much better by the ab initio unrestricted Hartree–Fock calculations than by the DFT calculations.

The structure can be viewed as a hydrogen-bond chain based on two relatively weak contacts, $\text{N1B}–\text{H1B} \cdots \text{O1W}$ and $\text{O1W}–\text{H1W1} \cdots \text{O2A}^{(ii)}$. Analysis of the magnetic properties confirms that this hydrogen-bond chain does not provide a magnetic exchange pathway because of the rather long intermolecular Ni–Ni separations.

The title complex efficiently prevents the growth of *P. verrucosum* fungus and is a versatile reproduction inhibitor for *E. coli*, *P. fluorescens*, *B. subtilis*, and *S. marcescens*. The antibacterial activity of **1** $[\text{Ni}(\text{Im})_2(\text{L-tyr})_2] \cdot 4\text{H}_2\text{O}$ is strongly correlated with the presence of imidazole in its structure.

■ ASSOCIATED CONTENT

S Supporting Information. X-ray crystallographic data in CIF format for **1** and details of the DFT and UHF calculations, tables, and supplementary figures. This material is available free of charge via the Internet at <http://pubs.acs.org>. Crystallographic data for **1** have also been deposited with the Cambridge Crystallographic Data Centre and are available at www.ccdc.cam.ac.uk/data_request/cif under deposition number CCDC 765515.

■ AUTHOR INFORMATION

Corresponding Author

*E-mail: agnieszka.wojciechowska@pwr.wroc.pl. Phone: +48 713203666. Fax: +48 71 320 43 60.

■ ACKNOWLEDGMENT

The authors are indebted to the Chemistry Department, Wrocław University of Technology, for financial support (Grant 344113). The high-field EPR spectra were recorded at the NHMFL, which is funded by the NSF through the Cooperative Agreement DMR-0654118, the State of Florida, and the DOE. The magnetic measurements were supported by the Polish Ministry of Science and Higher Education through Grant N N204 013936.

■ REFERENCES

- (1) Hamalainen, R.; Lajunen, K.; Valkonen, J. *Finn. Chem. Lett.* **1977**, 4–5, 108–112.
- (2) Kiss, T.; Gergely, A. *J. Chem. Soc., Dalton Trans.* **1984**, 1951–1957.
- (3) Molchanov, A. S.; Ledenkov, S. F. *Russ. J. Phys. Chem. A* **2009**, 28, 2028–2031.
- (4) Pettit, L. D. *Pure Appl. Chem.* **1984**, 56, 247–292.

- (5) (a) Mosset, A.; Bonnet, J. *J. Acta Crystallogr.* **1977**, B33, 2807–2812. (b) Yamauchi, O.; Odani, A.; Kohzuma, T.; Masuda, H.; Toriumi, K.; Sato, K. *Inorg. Chem.* **1989**, 28, 4066–4068. (c) Yamauchi, O.; Odani, A.; Masuda, H. *Inorg. Chim. Acta* **1992**, 198, 749–761. (d) Ramakrishna, S.; Rajendiran, V.; Palaniandavar, M.; Periasamy, V. S.; Sring, B. S.; Krishnamurthy, H.; Akbarsha, M. A. *Inorg. Chem.* **2009**, 48, 1309–1322.
- (6) Liu, W.; Song, Y.; Li, Y.; Zou, Y.; Dang, D.; Ni, Ch.; Meng, Q. *Chem. Commun.* **2004**, 20, 2348–2349.
- (7) (a) Wojciechowska, A.; Daszkiewicz, M.; Bienko, A. *Polyhedron* **2009**, 28, 1481–1489. (b) Zhang, S.; Hu, N.-H. *Acta Crystallogr.* **2009**, C 65, m7–m9. (c) Weng, J.; Hong, M.; Shi, Q.; Cao, R.; Chan, A. S. C. *Eur. Inorg. Chem.* **2002**, 2553–2556. (d) Apfelbaum-Tibika, F.; Bino, A. *Inorg. Chem.* **1984**, 23, 2902–2905. (e) Ye, Q.; Li, Y.-H.; Wu, Q.; Song, Y.-M.; Wang, J.-X.; Zhao, H.; Xiong, R.-G.; Xue, Z. *Chem.—Eur. J.* **2005**, 11, 988–994. (f) Facchin, G.; Torre, M. H. T.; Kremer, E.; Piro, O. E.; Castellano, E. E.; Baran, E. J. *J. Inorg. Biochem.* **2002**, 89, 174–180. (g) Wang, R.; Zheng, Z.; Jin, T.; Staples, R. J. *Angew. Chem., Int. Ed.* **1999**, 38, 1813–1815. (h) Li, D. Q.; Zhou, J.; Liu, X. *Acta Crystallogr.* **2007**, C63, m371–373.
- (8) Bruno, I. J.; Cole, J. C.; Edgington, P. R.; Kessler, M.; Macrae, C. F.; McCabe, P.; Pearson, J.; Taylor, R. *Acta Crystallogr.* **2002**, B58, 389–397 (CSD version 5.31).
- (9) (a) Hamalainen, R.; Ahlgren, M.; Turpeinen, U.; Raikas, T. *Cryst. Struct. Commun.* **1978**, 7, 379–384. (b) Pei, Y.; Wang, L. *Acta Crystallogr., Sect. E* **2006**, 62, m1668–m1670.
- (10) Sagiyan, A. S.; Babayan, E. E.; Geolchanyan, A. V.; Oganessian, A. M.; Pripadchev, D. A.; Maleev, V. I. *Armenian Chem. J.* **2007**, 60, 61.
- (11) Refat, M. S.; El-Korashy, S. A.; Ahmed, A. S. *J. Mol. Struct.* **2008**, 881, 28–45.
- (12) *CrysAlis RED, CrysAlis CCD (Version 1.171.30) and KM4CCD*; Oxford Diffraction Ltd.: Abingdon, Oxfordshire, U.K., 2004.
- (13) Sheldrick, G. M. *SHELXS97, Program for the Solution of Crystal Structures*; University of Göttingen: Göttingen, Germany, 1997.
- (14) (a) Sheldrick, G. M. *SHELXL97, Program for the Refinement of Crystal Structures*; University of Göttingen: Göttingen, Germany, 2008. (b) Sheldrick, G. M. *Acta Crystallogr.* **2008**, A64, 112–122.
- (15) (1) Myrczek, J. *Spectrosc. Lett.* **1990**, 23, 1027–1039. (b) Wojciechowska, A.; Staszak, Z.; Pietraszko, A.; Bronowska, W.; Cieślak-Golonka, M. *Polyhedron* **2001**, 21, 2063–2073. (c) Bierman, G.; Ziegler, H. *Anal. Chem.* **1986**, 58, 536–539.
- (16) Hassan, A. K.; Pardi, L. A.; Krzystek, J.; Sienkiewicz, A.; Goy, P.; Rohrer, M.; Brunel, L.-C. *J. Magn. Reson.* **2000**, 142, 300–312.
- (17) König, E. *Magnetic Properties of Coordination and Organometallic Transition Metal Compounds*; Springer-Verlag: Berlin, 1966.
- (18) Carballo, R.; Castineiras, A.; Covelo, B.; Garcia-Martinez, E.; Niclos, J.; Vazquez-Lopez, E. M. *Polyhedron* **2004**, 23, 1505–1518.
- (19) Murphy, B.; Aljabri, M.; Ahmed, A. M.; Murphy, G.; Hathaway, B. J.; Light, M. E.; Geilbrich, T.; Hursthouse, M. B. *Dalton Trans.* **2006**, 357–367.
- (20) Bernstein, J.; Davis, R. E.; Shimoni, L.; Chang, N. L. *Angew. Chem., Int. Ed. Engl.* **1995**, 34, 1555–1573.
- (21) Addison, A. W.; Rao, T. N.; Reedijk, J.; Van, Rijn, J.; Verschoor, G. C. *J. Chem. Soc., Dalton Trans.* **1984**, 1349–1356.
- (22) (a) Deacon, G. B.; Philips, R. J. *Coord. Chem. Rev.* **1980**, 33, 227–250. (b) Macrae, C. F.; Bruno, I. J.; Chisholm, J. A.; Edgington, P. R.; McCabe, P.; Pidcock, E.; Rodriguez-Monge, L.; Taylor, R.; van de Streek, J.; Wood, P. A. *J. Appl. Crystallogr.* **2008**, 41, 466–470. (c) Grell, J.; Bernstein, J.; Tinhofer, G. *Acta Crystallogr.* **1999**, B55, 1030–1043. (d) Grell, J.; Bernstein, J.; Tinhofer, G. *Acta Crystallogr.* **2000**, B56, 166. (e) Daszkiewicz M. *Struct. Chem.* **2011**, doi:10.1007/s11224-011-9872-2.
- (23) Wang, L.; Cai, J.; Mao, Z. W.; Feng, X. L.; Huang, J. W. *Trans. Met. Chem.* **2004**, 29, 411–418.
- (24) (a) Lever, A. B. P. *Inorganic Electronic Spectroscopy*; Elsevier: New York, 1984. (b) Martin, L. Y.; Sperati, C. R.; Busch, D. H. *J. Am. Chem. Soc.* **1977**, 99, 2968–2981. (c) Donini, J. C.; Hollebhone, B. R.; London, G.; Lever, A. B. P.; Hempel, J. C. *Inorg. Chem.* **1975**, 14,

- 455–461. (d) Daszkiewicz, M.; Staszak, Z.; Pietraszko, A.; Bronowska, W.; Cieslak-Golonka, M. *Struct. Chem.* **2006**, *17*, 599–608.
- (25) Perumareddi, J. R. *J. Phys. Chem.* **1972**, *76*, 3401.
- (26) Bernarducci, E.; Schwindinger, W. F.; Hughey, J. L.; Krogh-Jespersen, K.; Schugar, H. J. *J. Am. Chem. Soc.* **1981**, *103*, 1686–1691.
- (27) Merriam, J. S.; Perumareddi, J. R. *J. Phys. Chem.* **1975**, *79*, 142–149.
- (28) Pietraszko, A.; Bronowska, W.; Wojciechowska, A.; Staszak, Z.; Cieslak-Golonka, M. *Pol. J. Chem.* **2002**, *76*, 309–324.
- (29) Dobrzynska, D.; Jerzykiewicz, L. B.; Duczmal, M.; Wojciechowska, A.; Jablonska, K.; Palus, L.; Ozarowski, A. *Inorg. Chem.* **2006**, *45*, 10479–10486.
- (30) Ozarowski, A. *Inorg. Chem.* **2008**, *47*, 9760–9762.
- (31) Stoll, S.; Ozarowski, A.; Britt, R. D.; Angerhofer, A. *J. Magn. Reson.* **2010**, *207*, 158–163.
- (32) Krzystek, J.; Ozarowski, A.; Telser, J. *Coord. Chem. Rev.* **2006**, *250*, 2308–2324.
- (33) Collison, D.; Helliwell, M.; Jones, V. M.; Mabbs, F. E.; McInnes, A. J. L.; Riedi, P. C.; Smith, G. M.; Pritchard, R. G.; Cross, W. I. *J. Chem. Soc., Faraday Trans.* **1998**, *94*, 3019–3025.
- (34) Rogez, G.; Rebilly, J.-N.; Barra, A.-L.; Sorace, L.; Blondin, G.; Kirchner, N.; Duran, M.; Van Slageren, J.; Parsons, S.; Ricard, L.; Marvilliers, A.; Mallah, T. *Angew. Chem., Int. Ed.* **2005**, *44*, 1876–1879.
- (35) (a) Neese, F. *ORCA—an Ab Initio, Density Functional and Semiempirical Program Package*, version 2.8; Universität Bonn: Bonn, Germany, 2010. (b) Schaefer, A.; Horn, H.; Ahlrichs, R. *J. Chem. Phys.* **1992**, *97*, 2571–2577. (c) Ahlrichs, R.; et al., unpublished. (d) The Ahlrichs auxiliary basis sets were obtained from the *TurboMole* basis set library under <ftp.chemie.uni-karlsruhe.de/pub/jbasen>. (e) Eichkorn, K.; Treutler, O.; Ohm, H.; Haser, M.; Ahlrichs, R. *Chem. Phys. Lett.* **1995**, *240*, 283–289. (f) Eichkorn, K.; Weigend, F.; Treutler, O.; Ahlrichs, R. *Theor. Chem. Acc.* **1997**, *97*, 119–124. (g) Weigend, F.; Ahlrichs, R. *Phys. Chem. Chem. Phys.* **2005**, *7*, 3297.
- (36) Semenaka, V. V.; Nesterova, O. V.; Kokozay, V. N.; Dyakonenko, V. V.; Zubatyuk, R. I.; Shishkin, O. V.; Boca, R.; Jezierska, J.; Ozarowski, A. *Inorg. Chem.* **2010**, *49*, 5460–5471.
- (37) Makhankova, V. G.; Beznischenko, A. O.; Kokozay, V. N.; Zubatyuk, R. I.; Shishkin, O. V.; Jezierska, J.; Ozarowski, A. *Inorg. Chem.* **2008**, *47*, 4554–4563.
- (38) (a) Ye, S.; Neese, F.; Ozarowski, A.; Smirnov, D.; Krzystek, J.; Telser, J.; Liao, J.-H.; Hung, C.-H.; Chu, W.-C.; Tsai, Y.-F.; Wang, R.-C.; Chen, K.-Y.; Hsu, H.-F. *Inorg. Chem.* **2010**, *49*, 977–988. (b) Zein, S.; Neese, F. *J. Phys. Chem. A* **2008**, *112*, 7976–7983. (c) Zein, S.; Duboc, C.; Lubitz, W.; Neese, F. *Inorg. Chem.* **2008**, *47*, 134–142.
- (39) Ozarowski, A.; Zvyagin, S. A.; Reiff, W. M.; Telser, J.; Brunel, L. C.; Krzystek, J. *J. Am. Chem. Soc.* **2004**, *125*, 6574–6575.
- (40) (a) Krzystek, J.; Zvyagin, S. A.; Ozarowski, A.; Fiedler, A. T.; Brunold, T. C.; Telser, J. *J. Am. Chem. Soc.* **2004**, *126*, 2148–2155. (b) Sundararajan, M.; Ganyushin, D.; Ye, S.; Neese, F. *Dalton Trans.* **2009**, 6021–6036.
- (41) Boča, R. *Struct. Bonding (Berlin)* **2006**, *117*, 1–264.
- (42) Boča, R. *Coord. Chem. Rev.* **2004**, *248*, 757–815.
- (43) Thakur, G. A.; Shaikhi, M. M. *Acta Pol. Pharm. Drug Res.* **2006**, *63*, 95–100.
- (44) Islam, Md. R.; Islam, S. M. R.; Noman, A. S. M.; Khanam, J. A.; Ali, S. M. M.; Alam, S.; Lee, M. *Mycobiology* **2007**, *35* (1), 25–29.